

# Optics Letters

## III-V-on-silicon three-section DBR laser with over 12 nm continuous tuning range

SÖREN DHOORE,<sup>1,2,\*</sup> GUNTHER ROELKENS,<sup>1,2</sup> AND GEERT MORTHIER<sup>1,2</sup>

<sup>1</sup>Photonics Research Group, INTEC, Ghent University—IMEC, Ghent 9000, Belgium

<sup>2</sup>Center for Nano- and Biophotonics (NB-Photonics), Ghent University, Ghent 9000, Belgium

\*Corresponding author: Soren.Dhoore@UGent.be

Received 24 January 2017; accepted 17 February 2017; posted 22 February 2017 (Doc. ID 284159); published 9 March 2017

**Device and tuning characteristics of a novel heterogeneously integrated III-V-on-silicon three-section distributed Bragg reflector (DBR) laser are presented. The laser exhibits a continuous wavelength tuning range of more than 12 nm. Thermal tuning is achieved through carrier injection in the passive tuning layer of a III-V tunable twin-guide membrane. Single-mode lasing with a side-mode suppression ratio larger than 30 dB over the entire tuning range is realized through implementation of a sidewall-corrugated silicon-on-insulator waveguide grating as one of the laser mirrors.** © 2017 Optical Society of America

**OCIS codes:** (140.3600) Lasers, tunable; (140.5960) Semiconductor lasers; (230.1480) Bragg reflectors; (250.5300) Photonic integrated circuits.

<https://doi.org/10.1364/OL.42.001121>

Wavelength-tunable laser diodes have many potential applications, ranging from wavelength division multiplexing (WDM) systems in optical communication to beam-steering and spectroscopic remote sensing. In future advanced optical networks, they can be used as light sources to provide additional flexibility, wavelength-dependent routing, or bandwidth on demand [1,2]. They are also key components in emerging applications such as Light Detection and Ranging (LIDAR) and spectroscopy [3,4], in which flat-band continuous wavelength coverage is essential. In the past decade, different types of tunable laser diodes heterogeneously integrated on silicon-on-insulator (SOI) waveguides have been successfully demonstrated. The realization on SOI enables laser co-integration with passive silicon waveguide circuits, germanium photodetectors, and high-speed silicon modulators. Also, the large refractive index contrast in SOI allows for high optical confinement and small device footprints [5]. Tunable lasers can structurally be divided into two classes: distributed feedback (DFB)- and distributed Bragg reflector (DBR)-like devices. DFB types typically have a simpler device structure and require less tuning currents as compared to their DBR type counterparts, since no phase tuning section is needed to adjust the cavity mode location. In recent work, we demonstrated a discretely tunable III-V-on-silicon sampled grating (SG)-DFB laser with a discontinuous

tuning range of more than 55 nm [6]. However, DBR lasers offer a significant advantage in that optical gain, tuning, and feedback characteristics can be separately optimized because of the inherent different functionality in the longitudinal laser sections. Demonstrations of III-V-on-silicon tunable DBR-like lasers include a uniform-grating [7] and a single-ring [8] configuration with which 8 nm discontinuous wavelength tuning was obtained. With double-ring [9,10] configurations over 40 nm thermal tuning was achieved through exploitation of the Vernier effect. These laser structures, however, do not include a phase section and are more complex in terms of wavelength and power control.

In this Letter, we report on the demonstration of a novel III-V-on-silicon DBR laser that combines a III-V tunable twin-guide (TTG) membrane and a sidewall-corrugated SOI waveguide grating as narrowband spectral filter. A continuous wavelength tuning range of more than 12 nm is obtained with a side-mode suppression ratio (SMSR) greater than 30 dB. The maximum continuous-wave (CW) on-chip optical output power is 0.4 mW and varies less than 2 dB over the entire tuning range.

A 3D schematic of the overall laser structure is shown in Fig. 1. The laser consists of a passive SOI waveguide circuit on which a III-V TTG membrane [11] is heterogeneously integrated by means of adhesive divinylsiloxane-bis-benzocyclobutene (DVS-BCB) bonding [5]. The TTG membrane contains an InGaAsP double heterojunction active multiple quantum well (MQW) and a passive tuning layer in which carriers can be injected to provide optical gain and phase tuning, respectively. A 100-nm-thick *n*-InP separation layer electronically decouples both regions and serves as the common ground contact layer. The details of the full epitaxial layer stack are presented in Table 1. The laser cavity is formed by a broadband reflecting facet (reflectance ~30%) and a highly reflective DBR mirror (peak reflectance >90%). The latter is implemented as a first-order sidewall-corrugated waveguide grating [12] defined in the SOI device layer. The SOI waveguide structures are fabricated in a CMOS pilot-line at imec through deep UV lithography and have a 400-nm-thick silicon device layer with an etch depth of 180 nm. The DBR's weak sidewall corrugation provides a narrowband spectral reflection characteristic to ensure single-mode lasing operation. Ring resonator configurations do

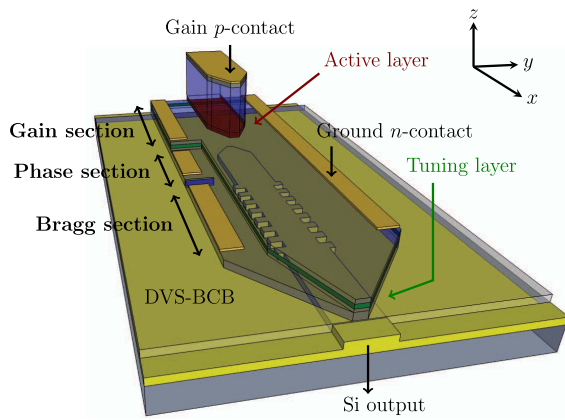


Fig. 1. 3D schematic of the III-V-on-silicon DBR laser.

Table 1. Tunable Twin-Guide Epitaxial Layer Stack

No.	Layer	Thickness	Doping
1	Substrate <i>n</i> -InP	500 $\mu\text{m}$	unknown
2	Stop-etch InGaAs	100 nm	n.i.d.
3	Sacrificial InP	100 nm	n.i.d.
4	Contact <i>p</i> -InGaAs	300 nm	$3 \times 10^{19} \text{ cm}^{-3}$
5	Cladding <i>p</i> -InP	1200 nm	$1 \times 10^{18} \text{ cm}^{-3}$
6	SCH InGaAsP	100 nm	n.i.d.
7	Well InGaAsP	$6 \times 8 \text{ nm}$	n.i.d.
8	Barrier InGaAsP	$5 \times 10 \text{ nm}$	n.i.d.
9	SCH InGaAsP	100 nm	n.i.d.
10	Cladding <i>n</i> -InP	100 nm	$5 \times 10^{18} \text{ cm}^{-3}$
11	Tuning InGaAsP	125 nm	n.i.d.
12	Cladding <i>p</i> -InP	50 nm	$1 \times 10^{18} \text{ cm}^{-3}$
13	Contact <i>p</i> -InGaAsP	100 nm	$5 \times 10^{18} \text{ cm}^{-3}$

offer high spectral purity but do not easily allow for a large free spectral range (FSR) due to minimum bend radii requirements. In the presented laser structure, three longitudinal sections can be discerned: a gain, a phase, and a Bragg section. In the gain section, current ( $I_{\text{gain}}$ ) is injected into the active layer to provide optical gain. The tuning layer is left unbiased. In the phase and Bragg sections, the active layer is removed during fabrication, and current ( $I_{\text{phase}}$  and  $I_{\text{Bragg}}$ , respectively) is injected into the tuning layer. Upon current injection, the effective index of the waveguide mode is modified through the free-carrier plasma dispersion effect ( $dn/dN < 0$ ) and Joule heating ( $dn/dT > 0$ ). Note that both effects are counteracting and lead to a blue and a red shift of the Bragg wavelength, respectively.

For the design of the SOI waveguide grating, a commercial mode solver from Lumerical Solutions is used. By anticipating lithographic fabrication errors, the design is precompensated by providing a stronger corrugation width  $\Delta W$  [see Fig. 2(a)] on the mask. A similar method is described in [13], in which a reduction of the grating coupling strength by a factor 3 is reported as a rule-of-thumb for a standard single-mode  $220 \text{ nm} \times 450 \text{ nm}$  SOI waveguide. Figures 2(a) and 2(b) show the SOI grating design and the fabricated structure, respectively. The grating coupling strength  $\kappa$  is estimated from  $\kappa = 2\Delta\bar{n}/\lambda_0$ , where  $\bar{n}$  represents the difference in the effective index for the fundamental mode considered in the wide and narrow waveguides, respectively.  $\lambda_0$  is the free-space wavelength. The simulated reflection spectra for the precompensated design and the

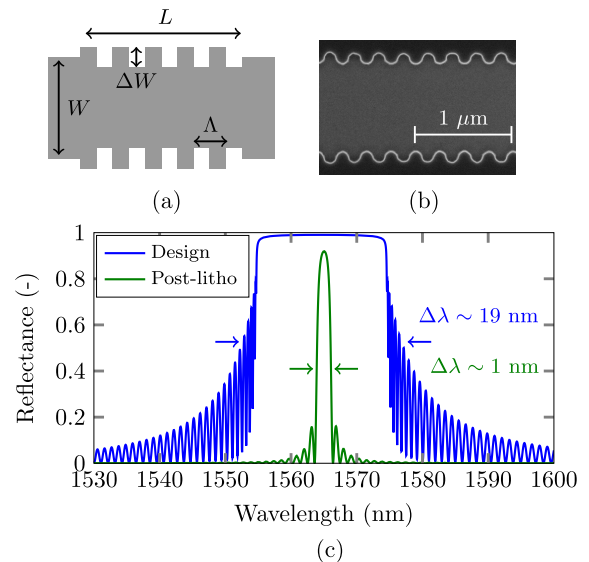
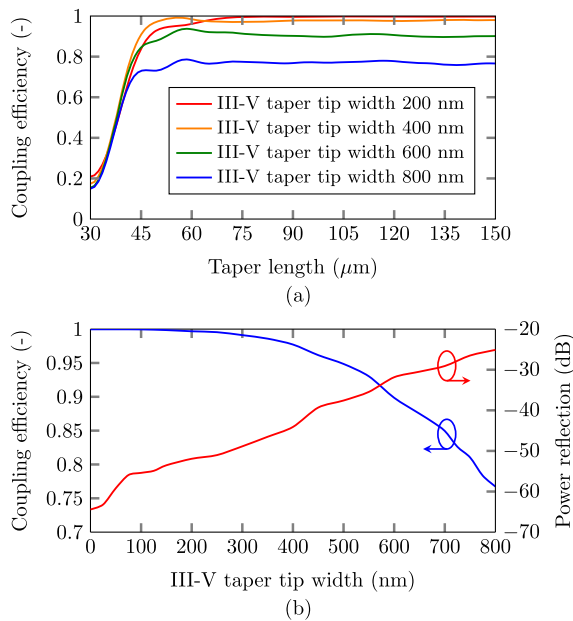


Fig. 2. Sidewall-corrugated SOI grating. (a) Design on the lithographic mask with  $L = 300 \mu\text{m}$ ,  $W = 1 \mu\text{m}$ ,  $\Delta W = 300 \text{ nm}$ , and  $\Lambda = 250 \text{ nm}$ . (b) SEM image of the fabricated structure. For clarity, the passive III-V tuning waveguide is not shown. (c) Simulated reflection spectra for the precompensated design and the fabricated structure (post-litho).

fabricated structure are shown in Fig. 2(c). The  $\kappa$  is significantly reduced from  $900/\text{cm}$  to  $70/\text{cm}$ , resulting in a targeted reflection characteristic with a 3 dB bandwidth  $\Delta\lambda$  of only 1 nm.

To efficiently couple light from the III-V waveguide to the output SOI waveguide, an adiabatic tapered coupler is used. The III-V waveguide and the SOI waveguide are inversely tapered down. In the first stage, the active III-V waveguide is tapered down from  $3 \mu\text{m}$  to  $1.5 \mu\text{m}$  over a short length of  $30 \mu\text{m}$ . In the second stage, the III-V waveguide is further tapered down to a narrow taper tip. The SOI waveguide is tapered up from  $200 \text{ nm}$  to  $1 \mu\text{m}$ . Note that the total thickness of the tuning layer and the surrounding cladding layers is not large enough to achieve phase matching between the active III-V waveguide mode and the passive III-V tuning waveguide mode. Therefore, light is immediately coupled from the active III-V waveguide to the underlying SOI waveguide. As the optical mode still has an evanescent tail in the passive III-V tuning waveguide, the tuning waveguide is tapered down as well in the third stage that comes after the phase and Bragg sections. Figure 3(a) shows the simulated coupling efficiency for the first and second taper stages as a function of taper length for different III-V taper tip widths. A DVS-BCB bonding layer thickness of  $50 \text{ nm}$  is assumed. It is clear that for taper lengths above  $90 \mu\text{m}$ , the coupling is already adiabatic, with a saturation of the coupling efficiency determined by the width of the III-V taper tip. To account for some robustness toward a lateral alignment offset between the III-V and SOI waveguide ( $0\text{--}200 \text{ nm}$ ) during optical contact lithography, a total taper length of  $130 \mu\text{m}$  is chosen. Figure 3(b) shows the influence of the III-V taper tip width on the coupling efficiency and the power reflection back into the waveguide for the chosen taper length. Although the coupling efficiency stays above 75% for III-V taper tips as wide as  $800 \text{ nm}$ , a III-V taper tip of  $400 \text{ nm}$  or narrower is required to keep the power reflection below  $-40 \text{ dB}$ , which is needed to prevent gaps in the wavelength tuning characteristics.



**Fig. 3.** III-V-to-silicon adiabatic tapered coupler. (a) Coupling efficiency for the first and second taper stages as a function of taper length. (b) Coupling efficiency and power reflection for the first and second taper stages as a function of III-V taper tip width for a total taper length of 130  $\mu\text{m}$ .

Fabrication of the laser devices starts with DVS-BCB-based adhesive bonding of the III-V TTG epitaxy on top of an SOI chip. Subsequently the  $n$ -InP substrate is removed and a silicon nitride hard mask is used to define the laser mesa. Afterwards, a combination of wet and dry etching is used to fabricate the desired laser cross section. A full description of the fabrication process for a standard III-V-on-silicon DFB laser can be found in [5]. In this case an additional lithography and dry etching step is needed to etch through the bottom  $n$ -InP,  $i$ -InGaAsP, and  $p$ -InP layers. Finally, the laser structure is planarized with DVS-BCB after which the metal contact pads are deposited. For the  $p$ -contacts and the  $n$ -contact, a Ti/Au and a Ni/Ge/Au metallurgy is used, respectively. Note that for the  $p$ -type tuning contacts in the phase and Bragg sections, highly doped  $p$ -InGaAsP (bandgap wavelength 1.3  $\mu\text{m}$ ) is utilized as contact layer material, which leads to only a small intervalence band absorption loss ( $\alpha_{\text{IVBA}, p\text{-InGaAsP}} \approx 10/\text{cm}$ ), given the relatively small confinement factor of 8% in the  $p$ -InGaAsP contact layer. For the  $p$ -contact in the gain section, highly doped  $p$ -InGaAs serves as the contact layer. Although the interband absorption coefficient is very high ( $\alpha \approx 10^4/\text{cm}$ , neglecting bandfilling effects), the modal loss is limited as the contact layer is separated by a 1.2- $\mu\text{m}$ -thick  $p$ -InP cladding layer from the MQW region, in which the optical mode is mainly confined. The laser facet is defined by means of a focused ion beam (FIB) cut to avoid the need for cleaving and that allows varying the cavity length from laser to laser. This, however, does not allow characterizing the laser from the low reflection facet side. An optical microscope image of the fabricated chip is shown in Fig. 4(c). The lengths of the gain (including the coupler), phase, and Bragg sections are 650  $\mu\text{m}$ , 100  $\mu\text{m}$ , and 300  $\mu\text{m}$ , respectively. The optical mode profiles in the phase and Bragg sections and in the gain section are shown in Figs. 4(a) and 4(b), respectively.

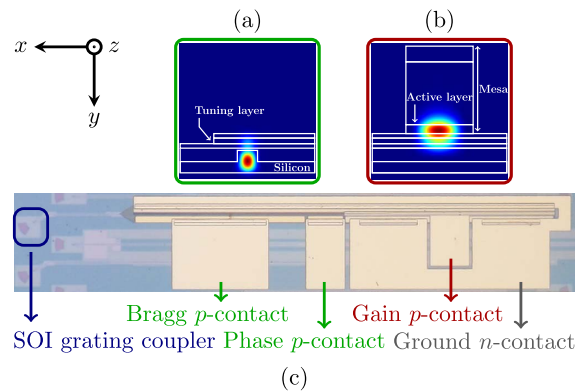


**Fig. 4.** (a) Optical mode profile in the phase and Bragg sections. (b) Optical mode profile in the gain section. (c) Optical microscope image of the fabricated laser device.

Device characterization is done on a temperature-controlled stage at 10°C. The DC electrical characteristics are measured with a current source and 4 electrical DC probes. The series resistances ( $dV/dI$ ) in the gain, phase, and Bragg sections are 4.5  $\Omega$ , 190  $\Omega$ , and 85  $\Omega$ , respectively. The resistance between the  $p$ -type phase and Bragg contacts is 5.4 k $\Omega$ . The optical properties are measured by coupling light from the chip to a standard single-mode optical fiber (SMF) by means of a reflectionless SOI grating coupler [14]. A power meter is used to measure the fiber-coupled optical output power. The measured fiber-to-chip coupling efficiency at the lasing wavelength is -15 dB. Figure 5 shows the light-current (LI) characteristic for the DBR laser when the phase and Bragg sections are left unbiased, i.e.,  $I_{\text{phase}} = I_{\text{Bragg}} = 0$  mA. The threshold current is 55 mA and the maximum CW on-chip optical output power is 0.4 mW. As expected this value is limited, as light is coupled out from the waveguide-grating side, which is designed to exhibit high reflectivity. Also note that facet fabrication is not optimal, which leads to a deterioration of the facet reflectivity and hence of the lasing threshold and optical output power. The peaks in the LI characteristic are due to longitudinal mode hopping. The lasing spectrum is measured by means of an optical spectrum analyzer at a resolution of 80 pm. The inset of Fig. 5 shows the optical spectrum, measured at  $I_{\text{gain}} = 120$  mA. The single-mode lasing operation is achieved at 1565 nm with a SMSR of 32 dB. The free spectral range

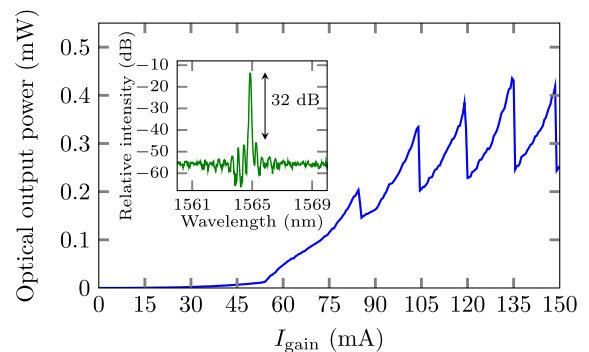


**Fig. 5.** Light-current (LI) characteristic for the DBR laser. The inset shows the optical spectrum at  $I_{\text{gain}} = 120$  mA. In both graphs,  $I_{\text{phase}} = I_{\text{Bragg}} = 0$  mA.

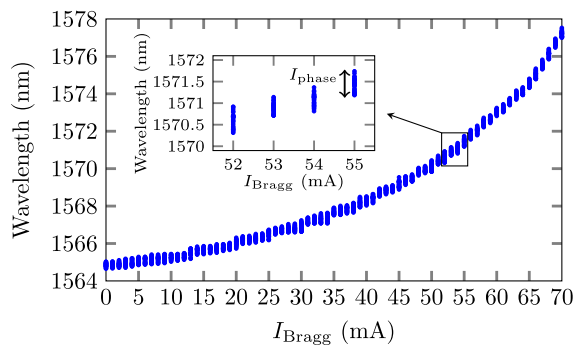


**Fig. 6.** Lasing wavelength as a function of  $I_{\text{Bragg}}$  at  $I_{\text{gain}} = 120$  mA.  $I_{\text{phase}}$  is varied between 0 mA and 24 mA. The current is swept in steps of 1 mA. The inset shows a close-up around 1571 nm, illustrating the continuous tuning nature.

(FSR) of the laser cavity is 0.5 nm. Wavelength tuning is done through carrier injection in the tuning layer of the phase and Bragg sections. Figure 6 shows the lasing wavelength as a function of  $I_{\text{Bragg}}$  when  $I_{\text{phase}}$  is varied between 0 and 24 mA. Clearly all wavelengths between 1565 nm and 1577 nm are accessible, and continuous tuning over the 12 nm wavelength range can be achieved through simultaneous adjustment of  $I_{\text{phase}}$  and  $I_{\text{Bragg}}$ . This is also illustrated in Fig. 7(a), which shows the lasing wavelength as a function of  $I_{\text{phase}}$  for different values of  $I_{\text{Bragg}}$ . When  $I_{\text{Bragg}}$  is kept fixed and  $I_{\text{phase}}$  is varied between 0 and 24 mA, at least two mode hops occur, which indicates that a  $2\pi$  phase shift can be achieved such that full wavelength coverage is possible. Figure 7(b) shows the

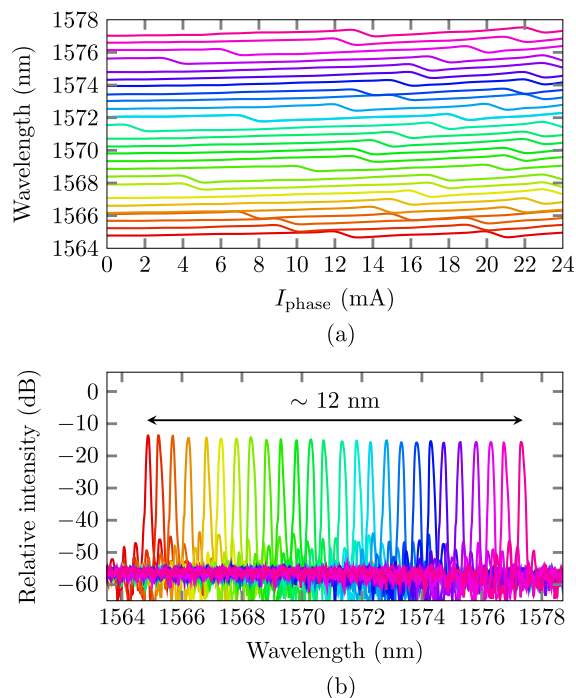


**Fig. 7.** (a) Lasing wavelength as a function of  $I_{\text{phase}}$ . (b) Superimposed lasing spectra for different  $I_{\text{phase}}$  and  $I_{\text{Bragg}}$ . In both graphs,  $I_{\text{gain}} = 120$  mA and  $I_{\text{Bragg}}$  is varied between 0 mA and 70 mA. The current step is chosen such that the peak wavelength spacing is 0.5 nm (also see Fig. 6).

superimposed lasing spectra across the tuning range. The SMSR remains larger than 30 dB and the optical output power varies only within 2 dB over the entire tuning range. The red shift of the lasing wavelength with increasing tuning current indicates a dominant heating effect. By improving the heat sinking and through a modification of the epitaxial layer stack (e.g., by using a thicker tuning and surrounding cladding layer) in future designs, we expect to significantly increase the optical confinement factor in the tuning layer, resulting in a stronger electronic effect and hence faster tuning ( $\sim$ ns). In that case, an adiabatic tapered III-V/SOI coupler design similar to one of the couplers reported in [15] can be used.

In conclusion, we have demonstrated a heterogeneously integrated III-V-on-silicon three-section DBR laser utilizing a sidewall-corrugated waveguide grating as a wavelength-selective mirror. A flat-band continuous tuning range of more than 12 nm is obtained with a SMSR greater than 30 dB and a maximum CW on-chip optical output power of 0.4 mW. The demonstrated laser device is expected to find application in future advanced optical networks and can be attractive for emerging applications, such as LIDAR and CO<sub>2</sub> spectroscopy.

**Funding.** Methusalem Programme of the Flemish Government.

## REFERENCES

1. L. G. Kazovsky, W.-T. Shaw, D. Gutierrez, N. Cheng, and S.-W. Wong, *J. Lightwave Technol.* **25**, 3428 (2007).
2. A. Le Liepvre, C. Simonneau, J.-C. Antona, C. Jany, A. Accard, F. Lelarge, D. Make, G.-H. Duan, and G. de Valicourt, *IEEE Photon. Technol. Lett.* **27**, 153 (2015).
3. G. J. Koch, J. Y. Beyon, F. Gibert, B. W. Barnes, S. Ismail, M. Petros, P. J. Petzar, J. Yu, E. A. Modlin, K. J. Davis, and U. N. Singh, *Appl. Opt.* **47**, 944 (2008).
4. G. Gao, B. Chen, and T. Cai, *Opt. Spectrosc.* **114**, 340 (2013).
5. G. Roelkens, A. Abassi, P. Cardile, U. Dave, A. De Groote, Y. de Koninck, S. Dhoore, X. Fu, A. Gassenq, N. Hattasan, Q. Huang, S. Kumari, S. Keyvaninia, B. Kuyken, L. Li, P. Mechet, M. Muneeb, D. Sanchez, H. Shao, T. Spuesens, A. Z. Subramanian, S. Uvin, M. Tassaert, K. Van Gasse, J. Verbist, R. Wang, Z. Wang, J. Zhang, J. van Campenhout, X. Yin, J. Bauwelinck, G. Morthier, R. Baets, and D. Van Thourhout, *Photonics* **2**, 969 (2015).
6. S. Dhoore, L. Li, A. Abbasi, G. Roelkens, and G. Morthier, *IEEE Photon. Technol. Lett.* **28**, 2343 (2016).
7. T. Ferrotti, B. Blampey, C. Jany, H. Duprez, A. Chantre, F. Boeuf, C. Seassal, and B. B. Bakir, *Opt. Express* **24**, 30379 (2016).
8. S. Keyvaninia, G. Roelkens, D. Van Thourhout, C. Jany, M. Lamponi, A. Le Liepvre, F. Lelarge, D. Make, G.-H. Duan, D. Bordel, and J.-M. Fedeli, *Opt. Express* **21**, 3784 (2013).
9. G.-H. Duan, C. Jany, A. Le Liepvre, A. Accard, M. Lamponi, D. Make, P. Kaspar, G. Levaufre, N. Girard, F. Lelarge, J.-M. Fedeli, A. Descos, B. Ben Bakir, S. Messaoudene, D. Bordel, S. Menezo, G. de Valicourt, S. Keyvaninia, G. Roelkens, D. Van Thourhout, D. J. Thomson, F. Y. Gardes, and G. T. Reed, *IEEE J. Sel. Top. Quantum Electron.* **20**, 158 (2014).
10. J. Hulme, J. Doylend, and J. Bowers, *Opt. Express* **21**, 19718 (2013).
11. M.-C. Amann, S. Illek, C. Schanen, and W. Thulke, *Appl. Phys. Lett.* **54**, 2532 (1989).
12. X. Wang, W. Shi, H. Yun, S. Grist, N. A. Jaeger, and L. Chrostowski, *Opt. Express* **20**, 15547 (2012).
13. L. Chrostowski and M. Hochberg, *Silicon Photonics Design: From Devices to Systems* (Cambridge University, 2015).
14. D. Vermeulen, Y. De Koninck, Y. Li, E. Lambert, W. Bogaerts, R. Baets, and G. Roelkens, *Opt. Express* **20**, 22278 (2012).
15. S. Dhoore, S. Uvin, D. Van Thourhout, G. Morthier, and G. Roelkens, *Opt. Express* **24**, 12976 (2016).